



HAL
open science

A comparison of a one-dimensional finite element method and the transfer matrix method for the computation of wind music instrument impedance

Robin Tournemenne, Juliette Chabassier

► **To cite this version:**

Robin Tournemenne, Juliette Chabassier. A comparison of a one-dimensional finite element method and the transfer matrix method for the computation of wind music instrument impedance. *Acta Acustica united with Acustica*, 2019, 105 (5), pp.838. 10.3813/AAA.919364 . hal-01963674v2

HAL Id: hal-01963674

<https://inria.hal.science/hal-01963674v2>

Submitted on 24 Oct 2019

HAL is a multi-disciplinary open access archive for the deposit and dissemination of scientific research documents, whether they are published or not. The documents may come from teaching and research institutions in France or abroad, or from public or private research centers.

L'archive ouverte pluridisciplinaire **HAL**, est destinée au dépôt et à la diffusion de documents scientifiques de niveau recherche, publiés ou non, émanant des établissements d'enseignement et de recherche français ou étrangers, des laboratoires publics ou privés.

A comparison of a one-dimensional finite element method and the transfer matrix method for the computation of wind music instrument impedance

Robin Tournemenne¹⁾, Juliette Chabassier¹⁾

¹⁾ Magique 3D Team, Inria Bordeaux Sud Ouest, 200 avenue de la vieille tour, 33405 Talence Cedex, France, firstname.lastname@inria.fr

1 Summary

This work presents a computation tool for the calculation of wind instrument input impedance in the context of linear planar wave propagation with visco-thermal losses. The originality of the approach lies in the usage of a specific **and simple 1D** finite element method (FEM). The popular Transfer Matrix Method (TMM) is also recalled and a seamless formulation is proposed which unifies the cases cylinders vs. cones. **Visco-thermal losses, which are natural dissipation in the system, are not exactly taken into account by this method when arbitrary shapes are considered. The introduction of an equivalent radius leads to an approximation that we quantify using the FEM method. The equation actually solved by the TMM in this case is exhibited. The accuracy of the two methods (FEM and TMM) and the associated computation times are assessed and compared.** Although the TMM is more efficient in lossless cases and for lossy cylinders, the FEM is shown to be more efficient when targeting a specific precision in the realistic case of a lossy trumpet. **Some additional features also exhibit the robustness and flexibility of the FEM over the TMM.** All the results of this article are computed using the open-source python toolbox OpenWind.

1 Introduction

The input impedance of wind instruments is defined as its frequency dependent linear response to an input excitation. This physical quantity is of considerable advantage in understanding the instrument's playing quality, and eventually its musical behavior [Campbell(2004), Chaigne and Kergomard(2016)]. The impedance is used for various purposes, such as the analysis of the instrument's playing properties, the synthesis of their sounds and the design of their shape. Indeed, many studies try to correlate the impedance features to the instrument actual intonation, stability, tone [Backus(1976), Braden et al.(2009), Campbell(2004)]. Many syn-

thesis methods rely on the input impedance knowledge to produce realistic sounds [Silva et al.(2014)], in order to assess the quality of the physical model, or to provide musicians with virtual instruments. Wind instrument design is the goal of many current initiatives, which try to either reconstruct bores, solve inverse problems based on their measured input impedance [Kausel(2001)], improve existing instruments [Tournemenne et al.(2017)] or even develop new instruments [Buys et al.(2017)] to fulfill the aspirations of musicians.

On the one hand, since the pioneering work of Webster [Webster(1947)], many methods can measure the input impedance with varying precision and frequency range [Le Roux et al.(2008), Caussé et al.(1984), Sharp et al.(2011)]. On the other hand, physical models associated with computation methods can be used to calculate the input impedance. The current reference computation method is the transfer matrix method (TMM), which has been used in the context of wind instruments for more than 40 years [Plitnik and Strong(1979), Mapes-Riordan(1993)]. The underlying physical model can assume plane or spherical wave propagation in the pipe, mono or multi-modal propagation, viscothermal losses at the pipe walls and a radiation impedance at the pipe output, etc.

The objective of this paper is to propose a new method for the computation of the input impedance, which could noticeably facilitate and broaden numerical instrument design approaches. It is not our purpose in this article to discuss the physical model and especially the validity of the underlying physical assumptions. Although this topic is of great interest, and must rely on precise simulation / measurement comparisons, the present work only focuses on technical aspects of the impedance computation. The methodology is here presented in the simplest possible realistic acoustical case, but the present article will serve as a basis to consider more general physical models in the future. We will present a new computation approach based on a one-dimensional finite element method used on the Telegraph equations with viscothermal losses. No-

85 tice first that, compared to the TMM, the proposed
 86 approach is therefore simply another way of solv-
 87 ing the same equations. Notice also that the objec-
 88 tive is not to solve the acoustical equations in 3D
 89 [Lefebvre and Scavone(2012)], nor the Navier-Stokes
 90 equations in 3D [Giordano(2014)]. The method pro-
 91 posed in this paper is close to finite difference methods
 92 [Bilbao(2009), van den Doel and Ascher(2008)], even
 93 if it is used here in the time-harmonic context.

94 This article goes in pair with an open-source
 95 Python 3 toolbox, Openwind [OpenWIND], that can
 96 be freely downloaded and used to undertake numerical
 97 experiments. After introducing the physical context
 98 in Section 2, the practical aspects of this numerical
 99 method (FEM) are first covered in Section 3, then
 100 the current reference method, the Transfer Matrix
 101 Method, is presented and its limits considering visco-
 102 thermal losses are exhibited in Section 4. A thorough
 103 validation is made in order to assess the precision
 104 and performance brought by this one-dimensional fi-
 105 nite element implementation in Section 5. The TMM
 106 can only approximate the solution when visco-thermal
 107 losses are considered for arbitrary shapes. We study
 108 the related error using the introduced FEM in Section
 109 6. Finally, computation times and several useful fea-
 110 tures of the FEM are presented (Section 6.3) before
 111 concluding.

112 2 Physics-based model

113 Consider an axisymmetric pipe occupying a domain
 114 $\Omega \subset \mathbb{R}^3 = (Ox, Oy, Oz)$ of slowly varying cross section
 115 S and rigid walls developing along the x axis, filled
 with air, see Figure 1.

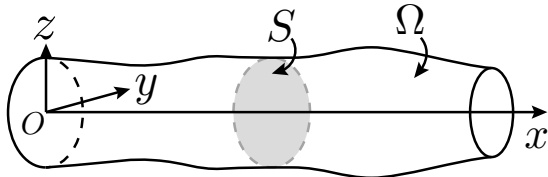


Figure 1: Definition of the space variables. S is the slowly varying section of the axisymmetric pipe.

116 The acoustic pressure $p(x, y, z, t)$ and the three-
 117 dimensional flow $u(x, y, z, t)$ can be considered as
 118 the solution to Navier-Stokes three-dimensional
 119 equations which induce an undue computa-
 120 tional burden in the context where only the
 121 wave propagating phenomena are of interest.
 122 Following the simplifications of Kirchhoff's the-
 123 ory regarding visco-thermal losses near the pipe
 124 walls [Kirchhoff(1868), Zwikker and Kosten(1949),
 125 Chaigne and Kergomard(2016)], the pressure can be
 126 considered as constant in the sections orthogonal
 127 to the x -axis, the orthogonal components of the
 128

| |
|---|
| Sound velocity: $c = 331.45\sqrt{T/T_0}$ m s ⁻¹ |
| Density: $\rho = 1.2929 T_0/T$ kg m ⁻³ |
| Viscosity: $\mu = 1.708 e - 5(1 + 0.0029 t)$ kg m ⁻¹ s ⁻¹ |
| Thermal conductivity: $\kappa = 5.77 e - 3(1 + 0.0033 t)$ Cal/(ms °C) |
| Spec. heat with constant p.: $C_p = 240$ Cal/(kg °C) |
| Ratio of specific heats: $\gamma = 1.402$ |

Table 1: Numerical values [Chaigne and Kergomard(2016)] of air constants used in the model. t is the temperature in Celsius, and T the absolute temperature with $T_0 = 273.15$ K.

three-dimensional flow can be neglected in the equa-
 129 tions while the axial component can be considered
 130 as axisymmetric with an analytic expression of its
 131 radial dependency. Finally, we seek in the frequency
 132 domain $\hat{p}(x, \omega)$ the acoustic pressure¹ and $\hat{u}(x, \omega)$ the
 133 volume flow, such that the one-dimensional interior
 134 equations read, for all position $x \in [0, L]$ and angular
 135 frequency $\omega \in [\omega_{\min}, \omega_{\max}]$,
 136

$$\begin{cases} Z_v(\omega, x) \hat{u} + \frac{d\hat{p}}{dx} = 0, & (1a) \\ Y_t(\omega, x) \hat{p} + \frac{d\hat{u}}{dx} = 0, & (1b) \end{cases}$$

$$(2) \begin{cases} Z_v(\omega, x) = \frac{j\omega\rho}{S(x)} [1 - \mathcal{J}(k_v(\omega)R(x))]^{-1}, \\ Y_t(\omega, x) = \frac{j\omega S(x)}{\rho c^2} [1 + (\gamma - 1)\mathcal{J}(k_t(\omega)R(x))], \end{cases}$$

$$k_v(\omega) = \sqrt{j\omega\frac{\rho}{\mu}}, \quad k_t(\omega) = \sqrt{j\omega\rho\frac{C_p}{\kappa}},$$

where R is the section radius, $S = \pi R^2$ is the section area, Table 1 describes the air constants, and we introduce the function \mathcal{J} of a complex variable, which models the dissipative terms, as

$$\mathcal{J}(z) = \frac{2 J_1(z)}{z J_0(z)}, \quad \forall z \in \mathbb{C}, \quad (3)$$

where J_0 and J_1 are the Bessel functions of the first
 137 kind. The subscripts v and t respectively stand for
 138 viscous and thermal dissipative phenomena.
 139

Furthermore, if the dissipative terms are neglected
 140 (\mathcal{J} function set to zero in the equations), the classical
 141 horn equations describing plane wave propagation in
 142 an axisymmetric lossless pipe can be retrieved from
 143 an asymptotic analysis from Euler's equations in a
 144 pipe with a slowly varying section [Rienstra(2005)].
 145 For convenience, we will use the names lossy model
 146 for system (1), and lossless model when \mathcal{J} is set to
 147 zero in system (1).
 148

Two boundary conditions complete the problem: at the bell $x = L$, we impose a radiation impedance condition

¹variables with a hat ($\hat{\cdot}$) denote the time-domain Fourier transform of the unknown

[Rabiner and Schafer(1978), Dalmont et al.(2001), Chaigne and Kergomard(2016)]:

$$\frac{\hat{p}(L, \omega)}{\hat{u}(L, \omega)} = Z_R(\omega), \quad (4)$$

and at the input of the pipe, we impose $\hat{u}(0, \omega) = \lambda(\omega)$, where $\lambda(\omega)$ will be a source term for the system. Since all the considered equations are linear, we can consider without loss of generality $\lambda(\omega) \equiv 1$. In this article, we are interested in computing the input impedance

$$Z(\omega) := \frac{\hat{p}(0, \omega)}{\hat{u}(0, \omega)} = \hat{p}(0, \omega). \quad (5)$$

Finally, the considered problem is the following: compute

$$Z(\omega) = \hat{p}(0, \omega), \quad \text{where} \quad (6)$$

$$\begin{cases} \left\{ \begin{array}{l} Z_v(\omega, x) \hat{u} + \frac{d\hat{p}}{dx} = 0, \\ Y_t(\omega, x) \hat{p} + \frac{d\hat{u}}{dx} = 0, \end{array} \right. & \forall x \in [0, L] \end{cases} \quad (7a)$$

$$\hat{u}(0, \omega) = 1, \quad (7b)$$

$$\begin{cases} \frac{\hat{p}(L, \omega)}{\hat{u}(L, \omega)} = Z_R(\omega). \end{cases} \quad (7c)$$

In the subsequent sections, we are interested in possible methods to solve system (7). We will first present the Finite Element Method and then the Transfer Matrix Method.

3 Finite element method

The finite element method (FEM) relies on a variational formulation of the entire system in usual infinite dimensional Sobolev spaces [Brezis(2011)], followed by the definition of finite dimensional spaces in which we seek numerically the solution. Recall that the Sobolev spaces L^2 and H^1 can be physically interpreted as $f \in L^2([0, L])$ if f is squared integrable on $[0, L]$ and $f \in H^1([0, L])$ if its gradient is squared integrable. For first order formulations as the one of system (7) (flow / pressure), the theory [Courant and Hilbert(1965), Cohen (2000)] points towards the possible following framework. Find $\hat{p}_h \in V_h \subset H^1([0, L])$, $\hat{u}_h \in W_h \subset L^2([0, L])$, such that for all $q_h \in V_h$, $w_h \in W_h$,

$$\left\{ \begin{array}{l} \int_0^L \frac{j\omega\rho}{S} [1 - \mathcal{J}(k_v(\omega)R)]^{-1} \hat{u}_h \overline{w_h} + \int_0^L \frac{d\hat{p}_h}{dx} \overline{w_h} = 0 \end{array} \right. \quad (8a)$$

$$\left\{ \begin{array}{l} \int_0^L \frac{j\omega S}{\rho c^2} [1 + (\gamma - 1)\mathcal{J}(k_t(\omega)R)] \hat{p}_h \overline{q_h} - \int_0^L \frac{d\overline{q_h}}{dx} \hat{u}_h - \overline{q_h}(0)\lambda(\omega) + \frac{1}{Z_R(\omega)} \hat{p}_h(L) \overline{q_h}(L) = 0 \end{array} \right. \quad (8b)$$

where by-parts integrations of Equations (7a) have been performed, followed by the use of the boundary conditions to weakly give a value to $\hat{u}_h(0)$ and $\hat{u}_h(L)$. The complex conjugate of z is noted \bar{z} . Note that other choices of by-part integrations are possible, associated with other choices of functional spaces. The type of boundary conditions and source regularity usually guide this choice. In practice, we have chosen to use standard Lagrange finite elements, hence to define the spaces V_h and W_h as follows. Other choices are possible and impact the properties of the method.

The instrument is discretized into N elements $\{K_j\}_j$, delimited by $N + 1$ nodes that constitute the mesh. On each element K_j we consider $r + 1$ interior degrees of freedom called $\{\xi_{j,p}\}_{1 \leq p \leq r+1}$.

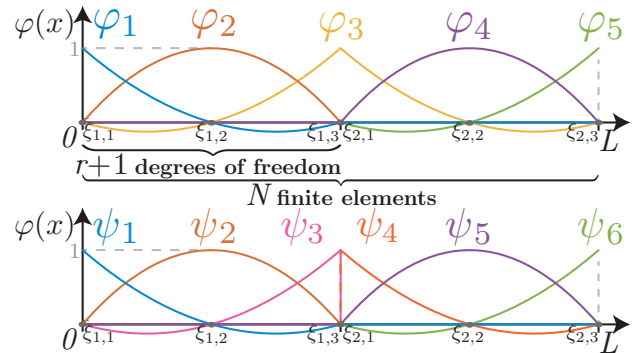


Figure 2: Basis functions with respect to x on a 2-elements mesh of $[0, L]$. Top : second order basis function $\{\varphi_i\}_{1 \leq i \leq 5}$ of V_h . Bottom : second order basis function $\{\psi_i\}_{1 \leq i \leq 6}$ of W_h . (colors online)

The finite dimensional spaces V_h and W_h are spanned by the nodal bases $\{\varphi_i\}_{1 \leq i \leq N_{H^1}}$ and $\{\psi_j\}_{1 \leq j \leq N_{L^2}}$ of piecewise polynomial functions of degree r (see an example of order 2 in Figure 2), which defines the order of the FEM. Consequently, the numerical solutions representing the pressure \hat{p}_h and volume flow \hat{u}_h are linear combinations of the basis functions $\{\varphi_i\}_{1 \leq i \leq N_{H^1}}$ and $\{\psi_j\}_{1 \leq j \leq N_{L^2}}$ respectively. In some communities, the basis functions are called shape functions. They are interpolation Lagrange polynomials (drawn Figure 2) associated to the concatenation of all the degrees of freedom of all the elements, where the nodes separating two elements are duplicated for W_h but not for V_h . Consequently, the basis functions of V_h are continuous while the ones of W_h present a discontinuity at the edges of the elements. This follows the conformal nature of the approximation, namely $V_h \subset H^1([0, L])$ and $W_h \subset L^2([0, L])$. Moreover, $N_{H^1} < N_{L^2}$ as soon as the mesh is composed of more than two elements. Finally, the integral terms in Equations (8) are evaluated through a quadrature procedure [Quarteroni et al.(2007)]. Although a high order quadrature formula could be employed to ensure exact integration, we have chosen to follow the condensation procedure (also named mass-

lumping procedure) of spectral high order finite elements [Cohen(2004)]². This technique is divided into two joint steps: using the same points for the quadrature and the interpolation which leads to a diagonal mass matrix (condensation), and choosing as interpolation points the Gauss-Lobatto points which prevents accuracy loss of the condensation method and improves the global matrix conditioning. Approximate integrals that come from this procedure will be denoted f .

Since system (8) stands for every $w_h \in W_h$ and $q_h \in V_h$, it is equivalent to state that it stands for every basis vector of W_h and V_h . Besides, we abusively still denote \hat{u}_h (resp. \hat{p}_h) for the coordinates of \hat{u}_h (resp. \hat{p}_h) in the basis $\{\varphi_i\}_{1 \leq i \leq N_{H^1}}$ (resp. $\{\psi_j\}_{1 \leq j \leq N_{L^2}}$). Consequently, the discrete formulation equivalently takes the matrix form

$$\begin{cases} j\omega M_h^{L^2} \hat{u}_h + j\omega N_h^{L^2}(\omega) \hat{u}_h - B_h \hat{p}_h = 0 \\ j\omega M_h^{H^1} \hat{p}_h + j\omega N_h^{H^1}(\omega) \hat{p}_h + \frac{1}{Z_R(\omega)} \Sigma_h \hat{p}_h \\ + B_h^* \hat{u}_h - E_h = 0 \end{cases} \quad (9a)$$

where * designates the adjoint and

$$\begin{aligned} (M_h^{L^2})_{i,j} &= \int_0^L \frac{\rho}{S} \psi_i \psi_j, & (M_h^{H^1})_{i,j} &= \int_0^L \frac{S}{\rho c^2} \varphi_i \varphi_j, \\ (N_h^{L^2})_{i,j}(\omega) &= \int_0^L \frac{\rho}{S} \frac{\mathcal{J}(k_v(\omega)R)}{1 - \mathcal{J}(k_v(\omega)R)} \psi_i \psi_j, \\ (N_h^{H^1})_{i,j}(\omega) &= \int_0^L \frac{S}{\rho c^2} (\gamma - 1) \mathcal{J}(k_t(\omega)R) \varphi_i \varphi_j, \\ (B_h)_{i,j} &= - \int_0^L \psi_i \frac{d\varphi_j}{dx}, & (E_h)_i &= \varphi_i(0), \\ (\Sigma_h)_{i,j} &= \varphi_i(L) \varphi_j(L) \end{aligned}$$

Notice that $M_h^{L^2}$, $M_h^{H^1}$, $N_h^{L^2}(\omega)$, $N_h^{H^1}(\omega)$ and Σ_h are diagonal matrices, B_h is block diagonal where the blocks are full and of size $r \times r + 1$ and E_h is a vector with only one non zero entry. This discrete formulation defines the following linear system on the global unknown U_h :

$$\begin{aligned} A_h(\omega)U_h(\omega) &= L_h, & A_h(\omega) &= \begin{pmatrix} A_{11}(\omega) & A_{12}(\omega) \\ A_{21}(\omega) & A_{22}(\omega) \end{pmatrix}, \\ L_h &= \begin{pmatrix} 0 \\ E_h \end{pmatrix}, & U_h(\omega) &= \begin{pmatrix} \hat{u}_h \\ \hat{p}_h \end{pmatrix}(\omega) \end{aligned} \quad (10)$$

$$\begin{aligned} A_{11}(\omega) &= j\omega M_h^{L^2} + j\omega N_h^{L^2}(\omega) \\ A_{12}(\omega) &= -B_h, & A_{21}(\omega) &= B_h^* \\ A_{22}(\omega) &= j\omega M_h^{H^1} + j\omega N_h^{H^1}(\omega) + \frac{1}{Z_R(\omega)} \Sigma_h \end{aligned}$$

Notice that the matrix A_h is sparse and can therefore be inverted by using efficient sparse routines

²section 11.1.1 pp. 169 to 177

[scipySparse]³. Once this system is numerically solved, for a discrete set of values $\{\omega_i\}_{1 \leq i \leq N_\omega} \in [\omega_{min}, \omega_{max}]$, the input impedance is

$$\forall 1 \leq i \leq N_\omega, \quad Z_{FEM}(\omega_i) = L_h^* U_h(\omega_i), \quad (11)$$

which is the $(N_{L^2} + 1)$ th term of the vector $U_h(\omega_i)$.

It is possible to diminish the computational burden by performing some pre-computations based on the pipe geometry and propagation hypotheses, and by taking advantage of the geometrical and arithmetical structure of the matrix A_h and of the required output [Amestoy et al.(2000)], but this is out of the scope of the current article.

Finally, for a given frequency, the N_{L^2} first terms of U_h give an approximation of the velocity at every degree of freedom along the bore, while the N_{H^1} last terms give an approximation of the pressure.

The FEM presented in this paper is implemented in OpenWind [OpenWIND], an open source (GPLv3) Python 3 toolbox.

4 Transfer matrix method

The transfer matrix method (TMM) consists in writing relations between output and input acoustic variables of simple geometries (cylinders, cones, Bessel and exponential bores...) from the use of the propagation equations [Caussé et al.(1984), Plitnik and Strong(1979)]. Consequently, given a radiation impedance $Z_R(\omega)$ and discretizing the bore profile in a series of N_p parts, it is possible to compute the instrument's input impedance. Let $\{x_i\}_{0 \leq i \leq N_p}$ be the list of positions on the bore's axis defining all the parts (with $x_0 = 0$ and $x_{N_p} = L$). We also define $\hat{p}_i(\omega)$ and $\hat{u}_i(\omega)$ as approximations of the pressure and the volume flow calculated by the TMM at the positions x_i . When the TMM is exact, $\hat{p}_i(\omega) = \hat{p}(x_i, \omega)$ and $\hat{u}_i(\omega) = \hat{u}(x_i, \omega)$.

Formally, the relation between the input and the output of one part can be expressed as a 2×2 matrix $T_{i+1}(\omega)$:

$$\begin{pmatrix} \hat{p}_i(\omega) \\ \hat{u}_i(\omega) \end{pmatrix} = \begin{pmatrix} a_{i+1}(\omega) & b_{i+1}(\omega) \\ c_{i+1}(\omega) & d_{i+1}(\omega) \end{pmatrix} \begin{pmatrix} \hat{p}_{i+1}(\omega) \\ \hat{u}_{i+1}(\omega) \end{pmatrix} \quad (12)$$

$$= T_{i+1} \begin{pmatrix} \hat{p}_{i+1}(\omega) \\ \hat{u}_{i+1}(\omega) \end{pmatrix}. \quad (13)$$

We then deduce the relation between the input and the output of the pipe:

$$\zeta = \begin{pmatrix} \hat{p}_0(\omega)/\hat{u}_L(\omega) \\ \hat{u}_0(\omega)/\hat{u}_L(\omega) \end{pmatrix} = \prod_{i=1}^{N_p} T_i(\omega) \begin{pmatrix} Z_R(\omega) \\ 1 \end{pmatrix}. \quad (14)$$

³more precisely, scipy is linked to a BLAS (Basic Linear Algebra Subprogram) which depends on your operating system and what has been installed on the computer. All the results of this article have been computed using the BLAS/LAPACK intel MKL 2018 and the linear system resolutions use a SuperLU procedure.

252 where $\hat{u}_L(\omega)$ is the volume flow at the pipe end, and
 253 finally $Z_{\text{TMM}} = \frac{\zeta(1)}{\zeta(2)}$. The global transfer matrix is
 254 defined as the product of all the elementary matrices
 255 T_i . An implicit transmission condition is there-
 256 fore assumed, which is the continuity of the variables
 257 between all parts. In practice, the computation is
 258 done only for a discrete set of pulsations $\{\omega_j\}_{1 \leq j \leq N_\omega}$.
 259 In the sequel, we will only consider the TMM for
 260 cylinders and cones. Transfer matrices for other ge-
 261 ometries are available in the literature [Braden(2007),
 262 Chaigne and Kergomard(2016), Helie(2013)].

263 For the lossless propagation case, the equations
 264 can be solved analytically for cones and cylinders
 265 and therefore the TMM provides the exact input
 266 impedance. In the presence of viscothermal losses,
 267 **the dissipation terms depend non linearly on the bore**
 268 **radius**, see Equation (2). It turns out that exact ma-
 269 trices can only be derived for the cylinder and not for
 270 more complex parts for which the radius depends on
 271 the space variable ($\hat{p}_i(\omega) \neq \hat{p}(x_i, \omega)$). A first empiri-
 272 cal approach handles this difficulty for conical parts
 273 by approximating them as a succession of cylinders of
 274 increasing or decreasing radii [Caussé et al.(1984)].
 275 A second empirical approach proposes to discretize
 276 each conical part in N_{sub} smaller cone subdivisions,
 277 and to use on each subdivision the transfer matrix
 278 derived for the cone considering lossless propa-
 279 gation, replacing some parameters by their lossy
 280 counterparts [Chabassier and Tournemene(2019)]
 281 evaluated at a chosen intermediate radius
 282 R^\odot [Mapes-Riordan(1993), Braden(2007)]. For
 283 a bore initially made of N_p conical parts, the total
 284 number of actual transfer matrices to compute would
 285 be $N_{\text{TMM}} = N_p \times N_{sub}$.

286 Since the viscothermal losses depend non-linearly
 287 on the radius, no optimal value for R^\odot can be im-
 288 mediately derived. Possible choices are the average
 289 radius $R^\odot = (R_i + R_{i+1})/2$ [Mapes-Riordan(1993)]
 290 (where R_i and R_{i+1} are the input and output radii
 291 of the cone subdivision), or any other weighted aver-
 292 age [Chaigne and Kergomard(2016), Helie(2013)]. In
 293 this article, we choose $R^\odot = (2 \min(R_i, R_{i+1}) +$
 294 $\max(R_i, R_{i+1}))/3$, which seems to be used in some
 295 existing implementations of the TMM.

We show (see [Chabassier and Tournemene(2019)]
 for more details) that using the TMM with the ap-
 proximate matrix obtained with this strategy corre-
 sponds to actually solving analytically, **for the ap-**
proximated solutions \hat{u} and \hat{p} , the following system of
 equations:

$$Z_{\text{TMM}}(\omega) = \hat{p}(0, \omega), \text{ where } \forall i \in [1, N_{\text{TMM}}], \quad (15)$$

$$\left\{ \begin{array}{l} \left\{ \begin{array}{l} Z_v^i \hat{u} + \frac{d\hat{p}}{dx} = 0, \\ Y_t^i \hat{p} + \frac{d\hat{u}}{dx} = 0, \end{array} \right. \quad \forall x \in [x_i, x_{i+1}] \quad (16a) \\ \\ Z_v^i = \frac{j\omega \rho}{S} [1 - \mathcal{J}(k_v(\omega)R_i^\odot)]^{-1}, \quad (16b) \\ Y_t^i = \frac{j\omega S}{\rho c^2} [1 + (\gamma - 1)\mathcal{J}(k_t(\omega)R_i^\odot)], \quad (16c) \\ \hat{p}(x_{i-}) = \hat{p}(x_{i+}), \quad \hat{u}(x_{i-}) = \hat{u}(x_{i+}), \quad (16d) \\ R_i^\odot = (2 \min(R(x_i), R(x_{i+1})) + \\ \quad \max(R(x_i), R(x_{i+1}))) / 3, \quad (16e) \\ \hat{u}(0, \omega) = 1, \quad (16f) \\ \frac{\hat{p}(L, \omega)}{\hat{u}(L, \omega)} = Z_R(\omega). \quad (16g) \end{array} \right.$$

296 This problem is different from the continuous prob-
 297 lem (7) solved with the FEM. The difference lies in
 298 the approximation R^\odot inside the function \mathcal{J} for every
 299 interval $[x_i, x_{i+1}]$ and amounts to approximating the
 300 original equation coefficients with discontinuous ones.

Finally, we propose a formulation unifying the
transfer matrices of the cylinder and the cone, which
coincides in either cases to the ones of the liter-
ature [Mapes-Riordan(1993)], under visco-thermal
losses. It reads:

$$a_{i+1}(\omega) = a, \quad b_{i+1}(\omega) = b, \quad c_{i+1}(\omega) = c, \quad d_{i+1}(\omega) = d,$$

where

$$(17) \left\{ \begin{array}{l} a = \frac{R_{i+1}}{R_i} \cosh \Gamma \ell - \frac{\beta}{\Gamma} \sinh \Gamma \ell \\ b = \frac{R_i}{R_{i+1}} Z_c \sinh \Gamma \ell \\ c = \frac{1}{Z_c} \left[\left(\frac{R_{i+1}}{R_i} - \frac{\beta^2}{\Gamma^2} \right) \sinh \Gamma \ell + \frac{\beta^2 \ell}{\Gamma} \cosh \Gamma \ell \right] \\ d = \frac{R_i}{R_{i+1}} \left(\cosh \Gamma \ell + \frac{\beta}{\Gamma} \sinh \Gamma \ell \right) \end{array} \right.$$

where

$$\Gamma \equiv \Gamma(\omega, R^\odot) = \frac{j\omega}{c} \sqrt{\frac{1 + (\gamma - 1)\mathcal{J}(k_t(\omega)R_i^\odot)}{1 - \mathcal{J}(k_v(\omega)R_i^\odot)}},$$

$$Z_c \equiv Z_c(\omega, R^\odot) = \frac{\rho c}{S(x_i)} \sqrt{\frac{[1 + (\gamma - 1)\mathcal{J}(k_t(\omega)R_i^\odot)]^{-1}}{1 - \mathcal{J}(k_v(\omega)R_i^\odot)}}$$

and

$$\beta = \frac{R_{i+1} - R_i}{\ell R_i}, \quad (18)$$

301 where R_i and R_{i+1} are respectively the input and out-
 302 put radii of the interval, ℓ is the axial length of the
 303 interval, and R^\odot the previously defined quantity.

304 The transfer matrices for cylinders and cones in the
 305 lossless case can be similarly unified, it only requires
 306 to replace Γ by $j\omega/c$ and Z_c by $\rho c/S$.

307 The TMM presented in this paper is implemented
 308 in OpenWind [OpenWind].

5 Validation

Unless otherwise stated, all input impedances presented hereafter are numerically computed from 20 to 2000 Hz with a 1Hz step, the temperature is set to 25 °C, and we consider a **terminal** impedance that models radiation from an infinite plane baffle [Rabiner and Schafer(1978)]:

$$Z_R(\omega) = \frac{\rho c}{S(L)} \frac{j\omega}{\alpha + j\omega\beta}, \quad (19)$$

where $\alpha = 3c\pi/(8R)$ and $\beta = 9\pi^2/128$. Other flanges can be modelled with this impedance form, by adjusting consequently the coefficients α and β , with a corresponding frequency validity range. Any other choice of radiation impedance can be done, including experimental ones, provided that the associated system of equations is well posed, meaning that its real part must be non-negative [Chandler-Wilde(1997)]. The discussion about radiation impedances is out of the scope of this paper, but it is important to note that the following conclusions regarding convergence rates and accuracy do not depend on this choice.

In the following, the FEM meshes are constructed as follows. A target element size (TES) is chosen by the user. The instrument being described by a series of radii at different axial points, some of the instrument parts might be shorter than the TES, and some might be longer. The instrument parts longer than the TES are equally divided to only obtain elements smaller or equal to the TES. **The instrument parts shorter than the TES are described by only one element having the same size than the part.** For realistic instruments, any TES choice will produce a non-uniform mesh since the instrument parts are not necessarily commensurate. The ratio τ between the largest and smallest elements in a mesh is an indicator of this uniformity, and is equal to 1 for a uniform mesh.

Up to 8 geometries are studied in the following. One 20 cm cylinder with 5 mm radius (roughly corresponding to a trumpet leadpipe) is used to assess an error estimator for the lossy model. We use 5 different cones and one arbitrary simple discontinuous geometry to help analyze the TMM error for the lossy model. **These geometries share their dimensions with existing instruments or instruments parts. They are intentionally simple and have been selected in order to be highly sensible to visco-thermal losses (small radius or fast slope). Besides, a trumpet-like bore based on measurements of a real commercial trumpet is used to provide a realistic study of the lossless and lossy models.** Its bore is made of 9 cones to describe the mouthpiece, 4 cones for the leadpipe, 1 central cylinder and 20 cones for the bell (33 cones in total). Apart from the cylinder, the 7 other geometries are described in Figure 3. Notice that the 3 cones corresponding to the mouthpiece cup, backbore, and

the trumpet leadpipe parts would normally be inside the instrument and yet we consider here their input impedance with open air radiation.

Notice that the relative errors that will be considered in the following of this paper are consequent to the discretization of the equations, and must be distinguished from the model error that would induce a discrepancy between the simulations and physical experiments. Quantifying this discretization error allows to correctly interpret the results of simulations.

All the results are obtained with OpenWind [OpenWinD].

5.1 Case without dissipation

The TMM is numerically exact for the lossless model, and can therefore be taken as a reference in this case. Consequently, in order to assess the numerical quality of the FEM, we compute the relative error of the FEM solution to the reference solution obtained with the TMM, E_{TMM} , in the lossless case, defined as:

$$E_{\text{TMM}}(i) = \frac{\|Z_{i \text{ FEM}} - Z_{\text{TMM}}\|}{\|Z_{\text{TMM}}\|}, \quad (20)$$

where $Z_{i \text{ FEM}}$ is the impedance computed using the FEM at order i , and Z_{TMM} the impedance computed using the TMM, and $\|\cdot\|$ denotes the discrete ℓ^2 norm of a vector over all the considered frequencies.

The upper part of Figure 4 shows the logarithm of $E_{\text{TMM}}(i)$ with respect to the order i of the FEM for the specific case of the trumpet bore displayed in Figure 3.

The mesh is obtained by choosing a TES equal to 3.4 cm, which gives $N = 72$ elements, with a ratio $\tau = 17$. We observe that the FEM provides a solution that is closer and closer to Z_{TMM} as the order increases. After order 10 (which represents a total of 649 degrees of freedom for the H^1 variable, 1369 degrees of freedom in total), the impedance relative ℓ^2 error does not diminish anymore and is close to 2.6×10^{-12} , which is dominated by roundup errors in double precision as expected. In the sequel we will call this a “converged solution”. The linear convergence in logarithmic scale agrees with the finite elements theory which predicts an exponential order (spectral) convergence. The lower part of Figure 4 shows the logarithm of $E_{\text{TMM}}(i)$ with respect to the logarithm of the target element size (TES) of the mesh, for the different FEM orders 1 to 6. Since the trumpet bore is composed of very large and very small parts, the observed curves are not yet exhibiting asymptotic rates of convergence (we would need much smaller TES in this case). However, we observe that for a given TES (and therefore mesh), increasing the order of the FEM always diminishes the relative ℓ^2 error on the input impedance, achieving a precision that is difficult to reach by refining the mesh at a given order.

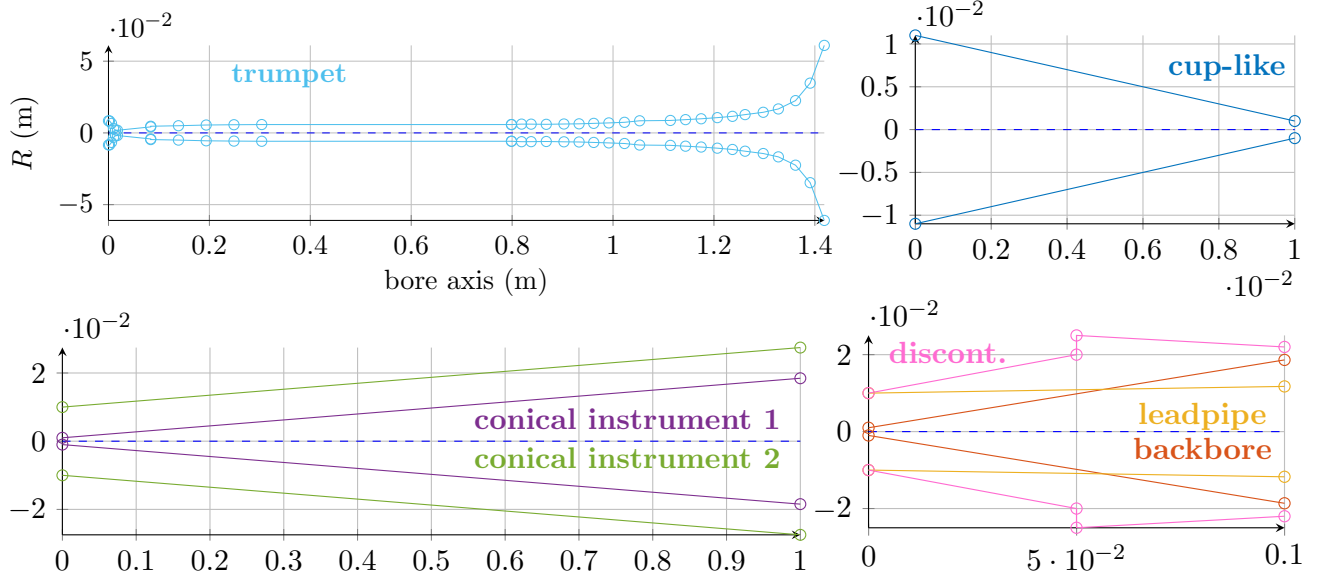


Figure 3: The seven studied bores. Top left : trumpet-like bore. Top right : simple convergent cone of general dimensions similar to a mouthpiece cup. Bottom left : two cones of 1m representative of conical instruments. Bottom right : two cones being qualitatively similar to a mouthpiece backbore and a trumpet leadpipe part, and one arbitrary geometry made of two cones, one divergent, the other convergent, and a clear discontinuity between them. The circles represent the extremities of each part. (colors online)

5.2 Case with dissipation

Regarding the model with viscothermal losses (lossy model), the TMM is exact for cylinders only. It will thus not be possible to use E_{TMM} to assess FEM convergence towards the exact solution for geometries of arbitrary shapes. Instead, we compute the relative ℓ^2 error between two finite element computations on the same mesh but consecutive orders:

$$E_{\text{order}}(i) = \frac{\|Z_{i+1}^{\text{FEM}} - Z_i^{\text{FEM}}\|}{\|Z_i^{\text{FEM}}\|}, \quad (21)$$

which is a heuristic and customary estimator when no exact solution is available (attributed to C. Runge, see [Repin(2008)]). Notice that it is not a mathematical *a posteriori* estimator [Babuska(1981), Ainsworth(1997)] but must be considered only as an illustration.

| order | 1 | 2 | 3 | 4 | 5+ |
|-------------------------------|-----|-----|------|-------|-------|
| frequential deviation (cents) | 236 | 26 | 0.3 | 0.01 | <1e-4 |
| amplitude deviation (dB) | 15 | 1.8 | 0.02 | 0.001 | <1e-5 |

Table 2: Frequential position and amplitude deviations of the second impedance peak of the 20cm cylinder (radius 5mm) using the lossy model. The reference is computed using the TMM. A visual representation of this second peak is shown Figure6.

The first considered case is a cylinder 20 cm long with a 5 mm radius, which could be compared qualitatively to a trumpet leadpipe in terms of dimensions.

In Figure 5, we consider a mesh of $N = 3$ elements and we represent both the E_{TMM} and the E_{order} relative ℓ^2 error estimators, since E_{TMM} is relevant in this case (it measures the distance to an exact solution). The two error estimators exhibit a very similar behavior which illustrates the fact that they are both relevant to assess the convergence of the FEM. In this case, the FEM provides a converged solution at order 9. The fact that E_{order} tends to machine precision illustrates the usual finite elements convergence theory [Fortin (1977), Cohen (2000)] which theoretically ensures that the obtained numerical solution is actually close to the exact impedance of the considered instrument (as opposed to a converged but false numerical solution) [Dauge et al.(2005)].

Figure 6 shows the modulus of the input impedance computation for the same cylinder with respect to the frequency, for different FEM orders. Table 2 gives the frequential and amplitude deviations of the second peak. The difference between the curves is visible for all orders, which is consistent with the fact that the solution is not yet converged. At a given order, the error increases with the frequency, which is known as the “pollution effect” [Gerdes and Ihlenburg(1999)]. When the order increases, the solution becomes valid in a wider frequency range. Two main effects are to be noted in the context of musical acoustics: the peaks amplitudes and frequencies can be wrong, the latter being due to numerical dispersion [Ihlenburg and Babuška(1995)]. Increasing the number of elements and/or the order allow to reduce these effects down to machine precision. In this case, at low

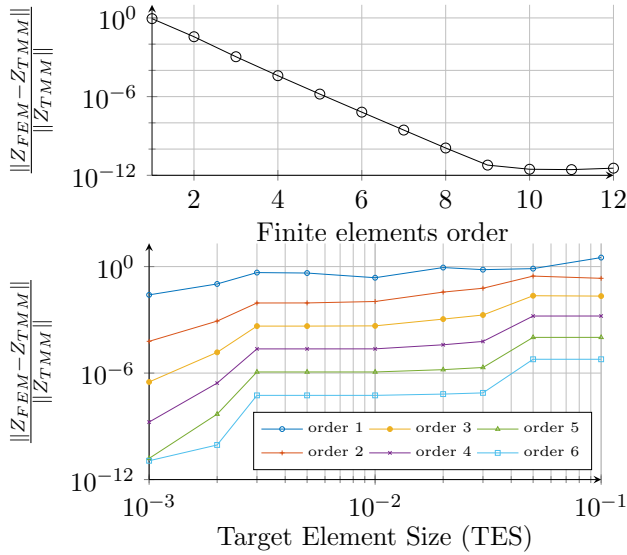


Figure 4: Relative ℓ^2 error between the input impedance obtained with the FEM and the TMM for the trumpet under lossless conditions. Top: the finite elements order varies on a given mesh, Bottom: the target element size (TES) varies for different FEM orders. (colors online)

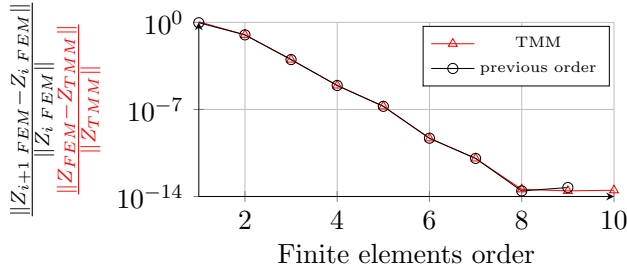


Figure 5: Comparison between E_{order} and E_{TMM} for a 20 cm cylinder of radius 5 mm using the lossy model. The FEM mesh is uniform with 3 elements.

445 orders of discretization, erroneous conclusions can be
446 drawn if the user does not attribute the dispersion to
447 the numerical approximation but to the model.

448 Notice finally that finite differences
449 [Bilbao and Chick(2013)] can be seen, at least
450 locally, as first order finite elements. The analyses of
451 Figures 4 and 6 illustrate the fact that using a first
452 order approximation can be a source of inaccuracy in
453 the context of musical acoustics.

454 Figure 7 shows the logarithm of the consecutive relative
455 ℓ^2 error E_{order} with respect to the FEM order,
456 considering the geometries of Figure 3, in the lossy
457 case. The number of elements is indicated in the leg-
458 end. An exponential order convergence is still ob-
459 served in the presence of dissipation which is in agree-
460 ment with the FEM theory **since only the coefficients**
461 **have changed**. Depending on the case, the solution
462 seems to be converged at an order ranging between 5
463 and 10, which is related to the properties of the cho-

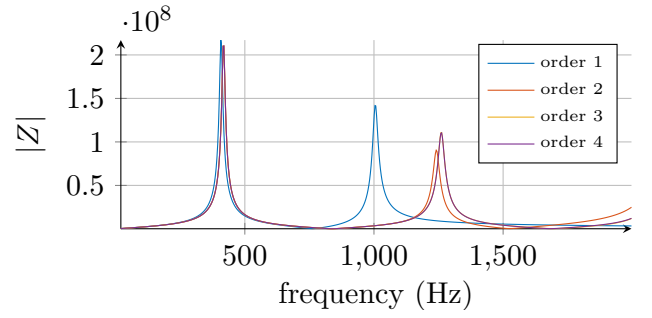


Figure 6: Modulus of the input impedance of a 20 cm cylinder of radius 5 mm computed by the FEM at different orders. (colors online)

464 sen mesh and to mathematical constants depending
465 on the exact solution.

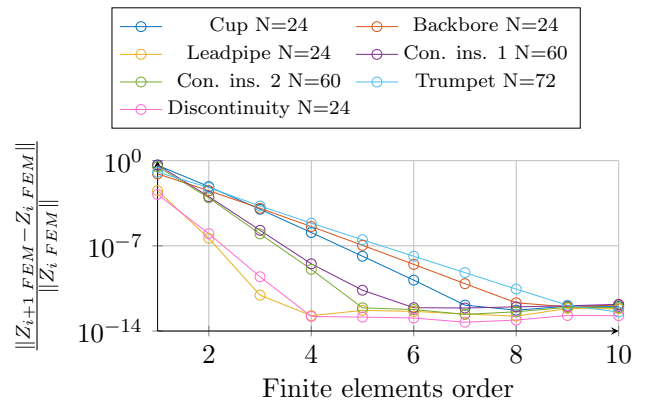


Figure 7: Consecutive relative ℓ^2 error between the input impedances obtained with the FEM for the lossy model using the bores of Figure 3 with respect to the FEM order. The number of elements of each mesh is given in the legend for each geometry. (colors online, matching with Figure 3)

6 Results

6.1 Study of the TMM error for arbitrary shapes considering losses

469 **Given the results of the previous sections, a converged**
470 **FEM solution can therefore be considered as the refer-**
471 **ence numerical solution for the lossy model, on geo-**
472 **metries for which no exact solution is available. As**
473 **said earlier, the TMM used on the lossy model is not**
474 **exact for bores of arbitrary shape, and follows an em-**
475 **pirical approach to compute input impedances, see**
476 **section 4. In this study, we investigate the second**
477 **empirical approach, subdividing every conical part in**
478 **N_{sub} equal segments and using for each subdivision**
479 **the formula (17), which amounts to solving the ap-**
480 **proximate Equations (16).**

481 It is possible to study the error made by the TMM

482 approximation, by computing the relative ℓ^2 error
483 with the converged FEM input impedance:

$$E_{\text{conv FEM}}(j) = \frac{\|Z_j \text{ TMM} - Z_{\text{conv FEM}}\|}{\|Z_{\text{conv FEM}}\|}, \quad (22)$$

484 where $Z_j \text{ TMM}$ is the input impedance computed using
485 the TMM with j subdivisions for each instrument
486 part, and $Z_{\text{conv FEM}}$ is the converged impedance obtained
487 by the FEM.

488 Since both methods solve different systems of equations
489 (namely, Equations (7) for the FEM and Equations (16)
490 for the TMM), the error between their solutions will be
491 related to the difference between their equations [Chabassier
492 and Tournemene(2019)]. As j increases, the TMM equations
493 tend to the FEM equations and thus we expect both solutions
494 to converge.

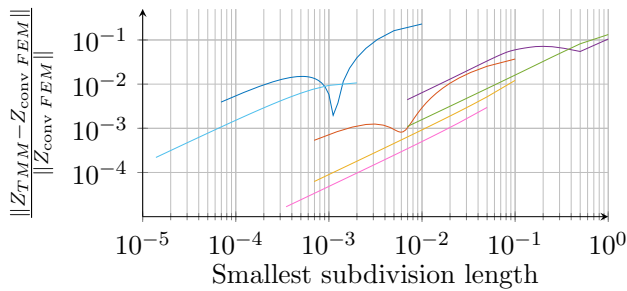


Figure 8: Relative ℓ^2 error between TMM solution and the converged FEM solution for the bores of Figure 3, w.r.t. the smallest subdivision length used for the TMM computation. (colors online, matching with Figure 3)

495 Figure 8 shows the logarithm of $E_{\text{conv FEM}}$ with
496 respect to the logarithm of the smallest subdivision
497 length Δx_j used to compute $Z_j \text{ TMM}$, for the different
498 bores displayed in Figure 3. The relative error is computed
499 on a frequency range of [20, 2000] Hz with a 1Hz step, but
500 the obtained results are similar when a different frequency
501 range is considered. A first observation is that all curves
502 are decreasing at rate close to 1 asymptotically (error
503 divided by 10 when the subdivisions length is divided by
504 10). For the first conical instrument, the mouthpiece backbore
505 and more extensively, for the cup-like bore, the curves show
506 a dip for a specific subdivision length value. This can
507 happen when considering few subdivisions for each cone and
508 disappears asymptotically, and can be interpreted as
509 fortuitous values of R^\ominus for the cones subdivisions.
510 More quantitatively, the error $E_{\text{conv FEM}}$ illustrates the
511 difference between the discretized TMM approach problem
512 (16) and the original system (7). Because the convergence
513 is slow (order 1 w.r.t. the subdivision length), the number
514 of TMM subdivisions needed to obtain a solution that has
515 converged up to machine precision is very large and induces
516 a very heavy computational cost.
517
518

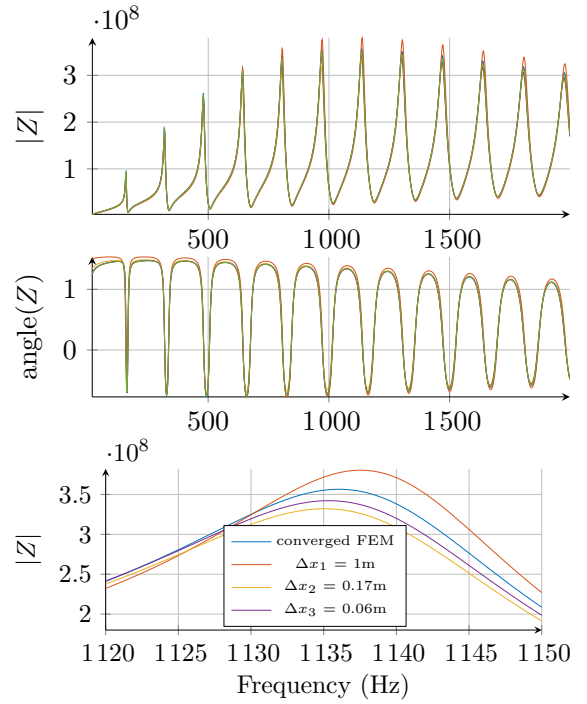


Figure 9: Impedance comparison between the converged FEM and the TMM method using different subdivision lengths of the Conical instrument 1. (colors online)

519 Figure 9 shows the input impedance of the instru-
520 ment Conical inst. 1 on the frequency range [0, 2]
521 kHz and [1120, 1150] Hz (close to the 7th impedance
522 peak). On this example, the amplitude and frequency
523 position of the impedance peaks are misjudged by the
524 TMM when the number of subdivisions is too low.
525 For example, the height of the 7th peak of this
526 instrument is 6.9% too low ($3.56e8$ against $3.32e8$) when
527 considering a subdivision length of 0.17 m (6 subdivi-
528 sions), and its frequency position is 1.37 cents too low
529 (1136Hz against 1135Hz). In the case of the cup-like
530 bore, this frequency shift is even higher (4.99 cents
531 for the first peak around 2000Hz with a subdivision
532 length of 0.01 m (1 subdivision) for the TMM).

533 6.2 Computation time and features 534 comparison of the two approaches

535 **Computation time** In the previous paragraphs,
536 we have seen that both the FEM and the TMM are
537 relevant to compute the input impedance of a given
538 instrument as defined in Equations (7). In order to com-
539 plete the methods' performance analysis, it is neces-
540 sary to assess and compare their computational costs.
541 Fast input impedance computation is especially use-
542 ful when considering optimisation applications where
543 a large number of input impedances must be com-
544 puted to reach optimal designs. Recall that the FEM
545 computation requires the inversion of the sparse lin-
546 ear system (10) while the TMM computation requires

the evaluation of the matrices product (14), both for a discrete set of pulsations $\{\omega_i\}_{1 \leq i \leq N_\omega}$. In the case of the FEM, most of the computation time is spent in computing the finite element matrices (10%), inverting them (39%), and evaluating the dissipative terms if any (48%) (these percentages depend somehow on the number of degrees of freedom). The matrices to invert are sparse and the overall conditioning of the matrices is good thanks to the use of spectral high order finite elements. A fair comparison can only be performed for numerical solutions that provide the same precision with respect to the exact solution. Since the FEM relies on the choice of both a mesh and an order, the same precision can be obtained with several situations that do not necessarily induce the same computational cost. In the sequel, the given time is always the smallest manually found computational time.

Firstly, for the cases where the TMM are exact (lossless case, lossy cylinder), the TMM computation is very competitive and provides the exact solution with only roundup errors. On the contrary, the FEM needs to be converged in order to provide a solution with a similar precision, and this induces an extra computational cost (about 1883 times more for the lossless trumpet and 194 times more for the lossy cylinder).

In the presence of viscothermal losses and arbitrary shapes, the TMM is not exact anymore and uses a discrete and empirical approach to compute the input impedance. We display in Figure 10 the computation times with respect to the relative ℓ^2 error to the converged solution, for the realistic trumpet-like bore⁴, for several TMM subdivision lengths (from $\Delta x = 2\text{e-}3\text{m}$ to $1.3\text{e-}5\text{m}$) and for the FEM with 35 elements at order 4.

Finally, Another FEM strategy called ‘‘adaptive’’ is also considered: it adapts the order of each mesh element to its size. This strategy avoids introducing too many degrees of freedom in small elements, improving the computation time without diminishing the global ℓ^2 error. In the specific case of the trumpet-like bore with a TES (Target Element Size) producing 35 elements, the first parts describing the mouthpiece are few millimeters long which is shorter than the TES. Consequently, the 4 interpolation points are unnecessarily cramped up on the only element of each of these parts. Therefore, a manual definition of the best order for each element, aided by the expected local shortest wavelength, is undertaken in order to obtain a good compromise between the number of degrees of freedom and the precision. In the example of Figure 10, the adaptive FEM improves the computation time by 11.1% compared with the usual FEM, and both computations lead to a relative ℓ^2 error of 4.1×10^{-4} .

The fastest TMM setting ($\Delta x = 2\text{e-}3\text{m}$), provides a

⁴Computations run on a 3.4GHz Intel Core i7-2600 with 16 GB of RAM

relative ℓ^2 error equal to 1.1% and computes the input impedance in 0.225 seconds, which is 11.2 times faster than the adaptive FEM (2.5 seconds). The most precise TMM setting has a precision similar to the FEM (2.2×10^{-4}), but the computation time is 11.9 times higher than the adaptive FEM (30.1s). Other orders (2, 3 and 5) have been considered for the mesh of 35 elements. Corresponding results are listed in Table 3 and the order 3 is displayed on Figure 10. All the computation times are similar (between 2 and 3.2 seconds) while the errors greatly improve (from $8.8\text{e-}2$ to $2.5\text{e-}5$). This shows the overall numerical performance of the FEM in real life situations, which can target a specific precision while maintaining a competitive computation time.

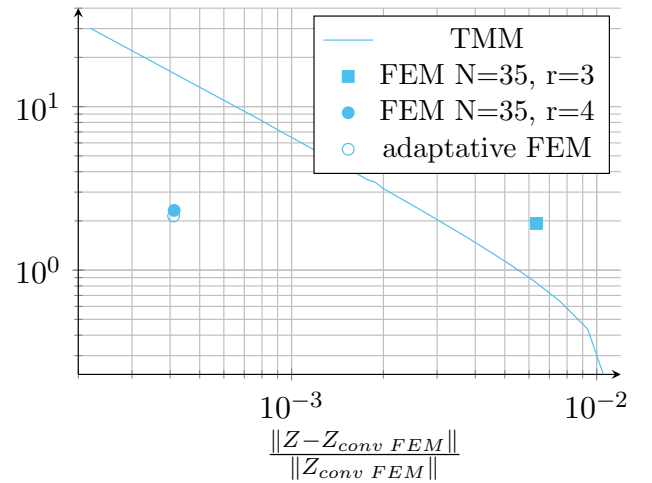


Figure 10: CPU time of the trumpet impedance computation w.r.t impedance relative ℓ^2 error. Comparison between the TMM and FEM methods.

| elements # | 35 | 35 | 35 | 35 |
|-----------------------|-----------------|-----------------|-----------------|-----------------|
| order | 2 | 3 | 4 | 5 |
| degrees of freedom | 105 | 140 | 175 | 210 |
| CPU time (s) | 2 | 2.4 | 2.8 | 3.2 |
| $E_{\text{conv FEM}}$ | $8.8\text{e-}2$ | $6.3\text{e-}3$ | $4.1\text{e-}4$ | $2.5\text{e-}5$ |

Table 3: Different computation times and $E_{\text{conv FEM}}$ considering different orders for the trumpet impedance using a 35 elements discretization.

Acoustic variables One immediate feature permitted by the FEM is the availability of the pressure and volume flow spectra along the entire bore axis, see Figure 11, which is directly obtained by considering all the vector U_h of system (10) (and not only the term corresponding to the input pressure). This output therefore comes at no extra computational cost compared to the impedance computation. Interpolation on arbitrary points is also possible without increasing the numerical error.

628 It could also be possible to reconstruct the pressure
 629 and volume flow using the TMM, but it would induce
 630 extra computational cost due to either over sampling
 631 of the bore profile (storing intermediate results of ma-
 632 trix products) or value interpolation (for which an ar-
 633 bitrary interpolation rule must be chosen and could
 potentially deteriorate the numerical result).

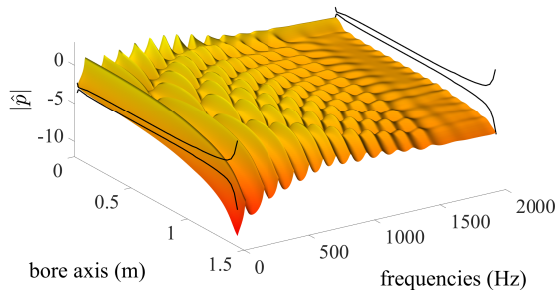


Figure 11: Evolution of the pressure modulus in logarithmic scale along the bore of the lossy trumpet according to frequency. The border at the beginning of the instrument (bore axis $x = 0$) displays the input impedance. (colors online)

634 In the case of a wind instrument, it helps to under-
 635 stand where the nodes and antinodes of the waves are
 636 located, which may help instrument makers better vi-
 637 sualize the instrument's functioning or even position
 638 the toneholes⁵.
 639

640 **Extended physical situations** One major advan-
 641 tage of using FEM over TMM is the possibility to
 642 easily solve equations with no available analytical so-
 643 lution while maintaining an arbitrary precision. In-
 644 deed, when more complex cases than lossless acous-
 645 tic propagation are considered, it may be impossi-
 646 ble to find analytical solutions, requiring the TMM
 647 to consider some approximations if possible (visco-
 648 thermal losses, continuously non-constant physical co-
 649 efficients). This feature could potentially give access
 650 to instruments impedances in very interesting phys-
 651 ical situations. For instance, it is theoretically and
 652 technically straightforward to consider non-constant
 653 physical coefficients, as in the case where the temper-
 654 ature varies inside the pipe. Indeed, this only prompts
 655 different values for the matrices $M_h^{L^2}$, $M_h^{H^1}$, $N_h^{L^2}(\omega)$
 656 and $N_h^{H^1}(\omega)$. Using exactly the same quadrature for-
 657 mulae, this only results in a different integrand taking
 658 into account the temperature value throughout the
 659 bore axis. The TMM can achieve a similar goal with
 660 less flexibility and less control on the discretisation
 661 error, refining the bore parts definition and consider-
 662 ing a different constant temperature on each refined
 663 parts.

⁵private discussion with the instrument maker Augustin Humeau

664 Table 4 shows the frequential position and ampli-
 665 tude deviations of the 9 first impedance peaks of
 666 the trumpet between a linear temperature gradient
 667 [Gilbert et al.(2006)] between 37 and 21 °C, and an
 668 averaged temperature of 29 °C inside the bore. There
 669 is a 7% difference between the two moduli of the
 670 impedances, showing the importance of the temper-
 671 ature gradient for impedance calculation. More pre-
 672 cisely, the frequential deviation varies between 0.3 and
 673 4.2 cents (1.9 cents in average), and the peaks ampli-
 674 tude varies between 0.1 and 0.3dB.

| peak # | 1 | 2 | 3 | 4 | 5 | 6 | 7 | 8 | 9 |
|-------------------------------|-----|-----|-----|-----|-----|-----|-----|-----|-----|
| frequential deviation (cents) | 4.2 | 1.5 | 1.4 | 1.7 | 2.6 | 1.5 | 1.4 | 2.1 | 0.3 |
| amplitude deviation (dB) | 0.1 | 0.2 | 0.2 | 0.3 | 0.3 | 0.2 | 0.2 | 0.2 | 0.1 |

Table 4: Frequential position and amplitude deviations between the two temperature profiles along the bore of the trumped for the lossy model, for the 9 first impedance peaks.

675 Other possibilities include the accurate considera-
 676 tion of arbitrary bores (Bessel, exponential, polynomi-
 677 als, splines, . . .), the possible integration of new terms
 678 in the equations or the coupling with other equations
 679 modelling different physical phenomena (pipes junc-
 680 tions, or excitators as lips, reeds, flue, . . .).

7 Conclusion and prospects

681 The precision and performances of FEM and TMM
 682 have been assessed, based on quantitative compari-
 683 son, as well as the exhibition of the actual equation
 684 solved by the TMM. In realistic cases as a trumpet
 685 with losses, the FEM allows to compute the same
 686 numerical solution as the TMM with a limited com-
 687 putational cost. It also allows to compute unusual
 688 physical situations as non-constant coefficients along
 689 the bore. Moreover, the computation gives a direct
 690 access to the acoustic variables inside the pipe for no
 691 extra computational cost or over-sampling. All the
 692 results of this article have been computed and can
 693 be run again using the open-source python toolbox
 694 OpenWind [OpenWInD]. Two direct extensions can
 695 follow this work: the implementation of toneholes in
 696 the model in order to model the input impedance of
 697 woodwind instruments, and the sound synthesis based
 698 on the same finite element method in space and finite
 699 difference in time. Notice that the presence of visco-
 700 thermal terms induces a major theoretical difficulty in
 701 the time domain [Berjamin et al.(2017)]. Finally this
 702 finite element framework is an efficient basis aiming at
 703 developing an inversion algorithm based on the full-
 704 waveform inversion [Virieux and Operto(2009)]. This
 705 technique can be used to optimize the instrument's
 706 geometry based on criteria derived from the input
 707 impedance, and relies strongly on the additional out-
 708

709 puts of the FEM impedance computation which are
710 the pressure and flow fields inside the instrument.

711 References

- 712 [scipySparse] “[https://docs.scipy.org/doc/
713 scipy/reference/sparse.html](https://docs.scipy.org/doc/scipy/reference/sparse.html)” .
- 714 [OpenWInD] “[https://gitlab.inria.fr/
715 openwind/release](https://gitlab.inria.fr/openwind/release) under GPLv3 licence
716 Chabassier, J., Tournemene, R.” .
- 717 [Ainsworth(1997)] Ainsworth, M. and Oden, J. T.
718 (1997). “A posteriori error estimation in finite
719 element analysis,” *Comput. Methods in Appl.
720 Mech. Eng.* **142**, 1–88.
- 721 [Amestoy et al.(2000)] Amestoy, P. R., Duff, I., and
722 L’Excellent, J.-Y. (2000). “Multifrontal par-
723 allel distributed symmetric and unsymmetric
724 solvers,” *Comput. Methods in Appl. Mech. Eng.*
725 **184**, 501–520.
- 726 [Babuska(1981)] Babuska, I. and Dorr, M. R. (1981).
727 “Error Estimates for the combined h and p ver-
728 sions of the finite element method,” *Numer.
729 Math.* **37**, 257–277.
- 730 [Backus(1976)] Backus, J. (1976). “Input impedance
731 curves for the brass instruments,” *The Journal
732 of the Acoustical Society of America* **60**(2), 470–
733 480.
- 734 [Berjamin et al.(2017)] Berjamin, H., Lombard, B.,
735 Vergez, C., and Cottanceau, E. (2017). “Time-
736 Domain numerical modeling of brass instruments
737 including nonlinear wave propagation, viscother-
738 mal losses, and lips vibration,” *Acta Acust
739 united Ac* **103**(1), 117–131.
- 740 [Bilbao(2009)] Bilbao, S. (2009). “Direct simulation
741 of reed wind instruments,” *Computer Music
742 Journal* **33**(4), 43–55.
- 743 [Bilbao and Chick(2013)] Bilbao, S., and Chick, J.
744 (2013). “Finite difference time domain simula-
745 tion for the brass instrument bore,” *J. Acoust.
746 Soc. Am.* **134**(5), 3860–3871.
- 747 [Braden(2007)] Braden, A. C. P. (2007). “Bore opti-
748 misation and impedance modelling of brass musi-
749 cal instruments,” Ph.D. thesis, University of Ed-
750 inburgh.
- 751 [Braden et al.(2009)] Braden, A. C. P., Newton,
752 M. J., and Campbell, D. M. (2009). “Trombone
753 bore optimization based on input impedance tar-
754 gets,” *J. Acoust. Soc. Am.* **125**(4), 2404–2412.
- 755 [Brezis(2011)] Brezis, H. (2011). “Functional analy-
756 sis, Sobolev spaces and partial differential equa-
757 tions,” (Springer New York, London).
- [Buys et al.(2017)] Buys, K., Sharp, D., and Laney,
758 R. (2017). “Developing and evaluating a hybrid
759 wind instrument,” *Acta Acust united Ac* **103**(5),
760 830–846. 761
- [Campbell(2004)] Campbell, M. (2004). “Brass in-
762 struments as we know them today,” *Acta Acust
763 united Ac* **90**(4), 600–610. 764
- [Caussé et al.(1984)] Caussé, R., Kergomard, J., and
765 Lurton, X. (1984). “Input impedance of brass
766 musical instruments—comparison between exper-
767 iment and numerical models,” *J. Acoust. Soc.
768 Am.* **75**(1), 241–254. 769
- [Chabassier and Tournemene(2019)] Chabassier, J.,
770 and Tournemene, R. (2019). “About the trans-
771 fert matrix method in the context of acoustical
772 wave propagation in wind instruments,” INRIA
773 Research Report 9254. 774
- [Chaigne and Kergomard(2016)] Chaigne, A., and
775 Kergomard, J. (2016). *Modern Acoustics and
776 Signal Processing “Acoustics of Musical Instru-
777 ments:”* (Springer New York). 778
- [Chandler-Wilde(1997)] Chandler-Wilde, S. N.
779 (1997). “The impedance boundary value prob-
780 lem for the Helmholtz equation in a half-plane,”
781 *Mathematical Methods in the Applied Sciences*
782 **20**, 813–840. 783
- [Cohen(2004)] Cohen, G. (2004). “Higher Order Nu-
784 merical Methods for Transient Wave Equations,”
785 (Springer, Berlin, Heidelberg). 786
- [Cohen (2000)] Cohen, G. and Fauqueux, S. (2000).
787 “Mixed finite elements with mass-lumping for the
788 transient wave equation,” *Journal of Computa-
789 tional Acoustics* **8** (1), 171–188. 790
- [Courant and Hilbert(1965)] Courant, R., and
791 Hilbert, D. (1965). “Methods of mathemat-
792 ical physics. partial differential equations,”
793 *Interscience* **2**. 794
- [Dalmont et al.(2001)] Dalmont, J.-P., Nederveen,
795 C. J., and Joly, N. (2001). “Radiation impedance
796 of tubes with different flanges: Numerical and ex-
797 perimental investigations,” *Journal of Sound and
798 Vibration* **244**(3), 505 – 534. 799
- [Dauge et al.(2005)] Dauge, M., Costabel, M., and
800 Schwab, C. (2005). “Exponential convergence of
801 hp-fem for maxwell’s equations with weighted
802 regularization in polygonal domains,” *Math.
803 Models Methods Appl. Sci.* **15**(4), 575–622. 804
- [Fortin (1977)] Fortin, M. (1977). “An analysis of the
805 convergence of mixed finite element methods,”
806 *RAIRO. Analyse Numérique* **11** (4), 341–354. 807

- [Gerdes and Ihlenburg(1999)] Gerdes, K., and Ihlenburg, F. (1999). “On the pollution effect in FE solutions of the 3D-Helmholtz equation,” *Computer Methods in Applied Mechanics and Engineering* **170**(1–2), 155–172.
- [Gilbert et al.(2006)] Gilbert, J., Ruiz, L. L., and Gougeon, S. (2006). “Influence de la température sur la justesse d’un instrument à vent,” in *Proceedings of Congrès Français d’Acoustique 2006, Tours*.
- [Giordano(2014)] Giordano, N. (2014). “Simulation studies of a recorder in three dimensions,” *J. Acoust. Soc. Am.* **135**(2), 906–916.
- [Helie(2013)] Hélie, Thomas and Hézard, Thomas and Mignot, Rémi and Matignon, Denis (2013). “One-dimensional acoustic models of horns and comparison with measurements,” *Acta Acust united Ac* **99**(6), 960–974.
- [Ihlenburg and Babuška(1995)] Ihlenburg, F., and Babuška, I. (1995). “Dispersion analysis and error estimation of galerkin finite element methods for the Helmholtz equation,” *Int. J. Numer. Methods Engrg.* **38**, 3745–3774.
- [Kausel(2001)] Kausel, W. (2001). “Optimization of brasswind instruments and its application in bore reconstruction,” *Journal of New Music Research* **30**(1), 69–82.
- [Kirchhoff(1868)] Kirchhoff, G. (1868). “Ueber den einfluss der wärmeleitung in einem gase auf die schallbewegung,” *Annalen der Physik* **210**(6), 177–193.
- [Le Roux et al.(2008)] Le Roux, J. C., Dalmont, J.-P., and Gazengel, B. (2008). “A new impedance tube for large frequency band measurement of absorbing materials,” *J. Acoust. Soc. Am.* **123**(5), 3119.
- [Lefebvre and Scavone(2012)] Lefebvre, A., and Scavone, G. P. (2012). “Characterization of woodwind instrument toneholes with the finite element method,” *The Journal of the Acoustical Society of America* **131**(4), 3153–3163.
- [Mapes-Riordan(1993)] Mapes-Riordan, D. (1993). “Horn modeling with conical and cylindrical transmission-line elements,” *J. Audio Eng. Soc.* **41**(6), 471–484.
- [Plitnik and Strong(1979)] Plitnik, G. R., and Strong, W. J. (1979). “Numerical method for calculating input impedances of the oboe,” *The Journal of the Acoustical Society of America* **65**(3), 816–825.
- [Quarteroni et al.(2007)] Quarteroni, A., Sacco, R., and Saleri, F. (2007). “Méthodes Numériques : Algorithmes, analyse et applications,” (Springer-Verlag Mailand).
- [Rabiner and Schafer(1978)] Rabiner, L. R., and Schafer, R. W. (1978). “Digital processing of speech signals,” **100** (Prentice-hall Englewood Cliffs, NJ).
- [Repin(2008)] Repin, S. (2008). “A Posteriori Estimates for Partial Differential Equations ,”, **Radon Series on Computational and Applied Mathematics** (Berlin, Boston: De Gruyter).
- [Rienstra(2005)] Rienstra, S. W. (2005). “Webster’s horn equation revisited,” *SIAM Journal on Applied Mathematics* **65**(6), 1981–2004.
- [Sharp et al.(2011)] Sharp, D., Mamou-Mani, A., and van Walstijn, M. (2011). “A single microphone capillary-based system for measuring the complex input impedance of musical wind instruments,” *Acta Acust united Ac* **97**(5), 819–829.
- [Silva et al.(2014)] Silva, F., Vergez, C., Guillemain, P., Kergomard, J., and Debut, V. (2014). “MoReeSC: A framework for the simulation and analysis of sound production in reed and brass instruments,” *Acta Acust united Ac* **100**(1), 126–138.
- [Tournemenne et al.(2017)] Tournemenne, R., Petiot, J.-F., Talgorn, B., Kokkolaras, M., and Gilbert, J. (2017). “Brass instruments design using physics-based sound simulation models and surrogate-assisted derivative-free optimization,” *Journal of Mechanical Design* **139**(4), 041401.
- [van den Doel and Ascher(2008)] van den Doel, K., and Ascher, U. M. (2008). “Real-time numerical solution of webster’s equation on a nonuniform grid,” *IEEE Transactions on Audio, Speech, and Language Processing* **16**(6), 1163–1172, doi: 10.1109/TASL.2008.2001107.
- [Virieux and Operto(2009)] Virieux, J., and Operto, S. (2009). “An overview of full-waveform inversion in exploration geophysics,” *Geophysics* **74**(6), WCC1–WCC26.
- [Webster(1947)] Webster, J. C. (1947). “An electrical method of measuring the intonation of cup-mouthpiece instruments,” *The Journal of the Acoustical Society of America* **19**(5), 902–906.
- [Zwikker and Kosten(1949)] Zwikker, C., and Kosten, C. W. (1949). “Sound absorbing materials,” (Elsevier).